PERGAMON

International Journal of Solids and Structures 40 (2003) 2521–2534

INTERNATIONAL JOURNAL OF SOLIDS and STRUCTURES

www.elsevier.com/locate/ijsolstr

Singular plastic fields in wedge indentation of pressure sensitive solids

Panos Papanastasiou [a,*], David Durban [b], Brian Lenoach [c]

[a] *Civil and Environmental Engineering, University of Cyprus, Nicosia 1678, Cyprus*
[b] *Faculty of Aerospace Engineering, Technion, Haifa 32000, Israel*
[c] *Schlumberger Cambridge Research, Cambridge CB3 0EL, UK*

Received 13 February 2002; received in revised form 25 November 2002

Abstract

The paper examines singular plastic fields induced near the tip of a wedge indentating a pressure sensitive solid. Plane strain conditions are assumed and material response is modelled by the small strain Drucker–Prager rigid/plastic constitutive law. A standard separation of variables solution is numerically generated for pure power-law hardening. Three possible measures of wall roughness are studied with an attempt to expose the coupling between wall friction and material pressure sensitivity. Sample calculations illustrate that stress singularity decreases with increasing friction, wedge angle and hardening exponent, but increases with pressure sensitivity. At large values of the hardening exponent, when the material is nearly perfectly plastic, effective stress contours approach the slip line limit. The concept of indentation index is introduced as a possible estimate for average indentation pressure.

Keywords: Wedge indentation; Pressure sensitive plasticity

1. Introduction

Wedge indentation processes in pressure sensitive plastic solids are encountered in numerous engineering applications ranging from geotechnical problems (pile foundations design, excavations) to sintered powder metals response in impact and penetration. However, while a considerable body of knowledge exists for wedges indentating metals, much less is available for the indenting process of porous materials. Two recent studies (Huang et al., 1998; Tordesillas and Shi, 1998) have examined and reviewed the wedge indentation process for the Mohr–Coulomb perfectly plastic solid. Interest in such a study arises from modelling hydraulic fracturing in soft rocks; a technique employed in oil industry to stimulate production of hydrocarbons by creating fractures around a wellbore (Papanastasiou, 1999). There is also considerable interest in the microelectronic industry in deformation and fracture of porous low-k dielectric films. Polymers are

* Corresponding author. Tel.: +357-22-892292; fax: +357-22-892254.
E-mail address: panospap@ucy.ac.cy (P. Papanastasiou).

0020-7683/03/$ - see front matter
doi:10.1016/S0020-7683(03)00019-2

pressure sensitive and can be modelled as viscoplastic solids below their glass transition temperature. An interesting study of microwedge indentation delamination has been given in De Boer and Gerberich (1996).

In this paper we use the rigid/plastic Drucker–Prager material model, formulated as a small strain deformation theory in conjunction with pure power-law response, to investigate near tip singular fields in wedge indentation. Concentrating on symmetric fields, with a plane strain pattern, we begin with an eigenvalue formulation for circumferential profiles of stresses and displacements. Wall friction is implemented in boundary data by three different, yet equivalent, laws employing the Coulomb friction coefficient f, the Prandtl friction factor m and a porosity friction factor ρ. These three measures of surface roughness are interrelated by a simple formula, and it turns out that while m is bounded by an upper limit, both f and ρ admit lower limits. For given m the corresponding values of (f,ρ) depend on wedge angle, hardening index and pressure sensitivity. These findings are compatible with results for the Mises solid (Durban, 1999).

Sample calculations illustrate that the level of stress singularity increases as the wedge becomes sharper and smoother. Strain hardening causes an increase in the singularity of stresses. Examples of effective stress contours indicate that with vanishing hardening, when the material approaches the perfectly plastic model, contours of effective stress, near the tip, approach the slip lines of perfect plasticity.

It is suggested that the present analysis can be useful in providing a simple approximate assessment of the average indentation pressure. To this end we have defined the indentation index in terms of singularity level and friction measures. A few special cases are derived for the indentation index at different degrees of approximation.

2. Near tip plastic field equations

With the notation of Fig. 1 we focus attention on the singular stress field which is expected to develop near the tip of a rigid wedge indenting a plastic medium under plane strain conditions. Material response within that singular plastic zone is given by the plastic branch of the associated Drucker–Prager solid (Durban and Papanastasiou, 1997)

$$\boldsymbol{\epsilon} = \epsilon_{\mathrm{p}}\left(\frac{3\mathbf{S}}{2q} + \frac{\mu\mathbf{I}}{3}\right) \tag{1}$$

where $\boldsymbol{\epsilon}$ is the small strain tensor, $\mathbf{S}$ is the stress deviator and $\mathbf{I}$ is the second order unit tensor. The effective stress, σ_{e} (identified with the plastic potential), is defined by

$$\sigma_{\mathrm{e}} = q + \mu\sigma_{\mathrm{h}} \tag{2}$$

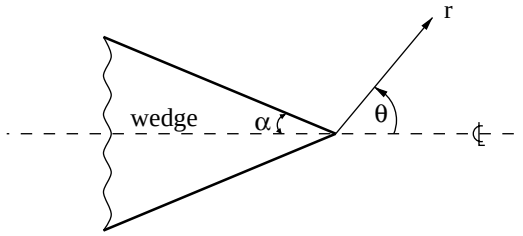

Fig. 1. Notation for plane strain wedge indentation.

with q and σ_h denoting the Mises effective stress and the hydrostatic stress, respectively, given by

$$q = \left(\frac{3}{2}\mathbf{S}\cdot\cdot\mathbf{S}\right)^{1/2} \quad \sigma_h = \frac{1}{3}\mathbf{I}\cdot\cdot\boldsymbol{\sigma} \quad \mathbf{S} = \boldsymbol{\sigma} - \sigma_h\mathbf{I} \tag{3}$$

Pressure sensitivity is reflected by the parameter μ with the Mises model recovered when $\mu = 0$. The total plastic strain in (1) is assumed to be a known function of the effective stress σ_e, with the specific power law employed in this study

$$\epsilon_p = \left(\frac{\sigma_e}{\sigma_0}\right)^n \tag{4}$$

where both the hardening exponent n and reference stress σ_0 are material parameters determined experimentally.

Following standard practice of singular plastic field analysis, we examine separation of variables representation of the stress components, within the near tip zone,

$$\sigma_r = r^s\tilde{\sigma}_r \quad \sigma_\theta = r^s\tilde{\sigma}_\theta \quad \sigma_{r\theta} = r^s\tilde{\sigma}_{r\theta} \quad \sigma_z = r^s\tilde{\sigma}_z \tag{5}$$

where s (expected to be negative) is the stress singularity level to be determined, and the tilde marks circumferential stress profiles (eigenfunctions) associated with the eigenvalue s.

Likewise, we shall use the separation of variables relations

$$q = r^s\tilde{q} \quad \sigma_h = r^s\tilde{\sigma}_h \quad \sigma_e = r^s\tilde{\sigma}_e \tag{6}$$

where, again, tilted quantities depend only on θ.

The plane strain constraint requires that all of the z components of the strain tensor (1) vanish, hence

$$(\tilde{\sigma}_z - \tilde{\sigma}_h) + \frac{2}{9}\mu\tilde{q} = 0 \tag{7}$$

while the shear stress components in the z-plane are identically zero. Combining (7) with the definition of q in (3) we find that

$$\tilde{q} = \frac{1}{m_{\max}}\left[\left(\frac{\tilde{\sigma}_r - \tilde{\sigma}_\theta}{2}\right)^2 + \tilde{\sigma}_{r\theta}^2\right]^{1/2} \quad \text{with } m_{\max} = \left(\frac{1 - \mu^2/9}{3}\right)^{1/2} \tag{8}$$

and

$$\tilde{\sigma}_h = \frac{1}{2}(\tilde{\sigma}_r + \tilde{\sigma}_\theta) - \frac{\mu}{9}\tilde{q} \tag{9}$$

Relations (8) and (9) give the circumferential profiles of the Mises stress and hydrostatic stress in terms of plane components of stress. Parameter $m_{\max}$, which will be discussed later, is the maximum local friction factor in the sense that when $\tilde{\sigma}_{r\theta} = \pm m_{\max}\tilde{q}$ the entire Mises stress is activated by $\tilde{\sigma}_{r\theta}$ with $\tilde{\sigma}_r = \tilde{\sigma}_\theta$. The circumferential profile of the effective stress σ_e follows in the form

$$\tilde{\sigma}_e = 3m_{\max}^2\tilde{q} + \frac{\mu}{2}(\tilde{\sigma}_r + \tilde{\sigma}_\theta) \tag{10}$$

with $\tilde{q}$ given in (8). Plane strain deformation is maintained if, by (7) and (9),

$$\tilde{\sigma}_z = \frac{1}{2}(\tilde{\sigma}_r + \tilde{\sigma}_\theta) - \frac{\mu}{3}\tilde{q} \tag{11}$$

The two equations of equilibrium, written in polar coordinates, for the plane components of stress, become in view of (5)

$$\tilde{\sigma}'_{r\theta} + (s+1)\tilde{\sigma}_r - \tilde{\sigma}_\theta = 0 \tag{12}$$

$$\tilde{\sigma}'_\theta + (s+2)\tilde{\sigma}_{r\theta} = 0 \tag{13}$$

where the prime denotes differentiation with respect to θ.

Turning to strains and displacements, we note from (4) and (6) that the total plastic strain can be written as

$$\epsilon_p = k r^{ns} \tilde{\sigma}_e^n \quad \text{with } k = \sigma_0^{-n} \tag{14}$$

We expect therefore that the (r,θ) components of the displacement—denoted by (u,v), respectively—can be represented, within the singular zone, as

$$u = k r^{ns+1} \tilde{u} \quad v = k r^{ns+1} \tilde{v} \tag{15}$$

where $(\tilde{u},\tilde{v})$ are the circumferential profiles of the displacements.

Finally, we insert the stresses (5), (6) and the displacements (15) in the tensorial constitutive relation (1). This gives, with the aid of (9), the three scalar equations

$$(ns+1)\tilde{u} = \tilde{\sigma}_e^n \left[\frac{3}{2\tilde{q}} \left(\frac{\tilde{\sigma}_r - \tilde{\sigma}_\theta}{2} \right) + \frac{\mu}{2} \right] \tag{16}$$

$$\tilde{u} + \tilde{v}' = \tilde{\sigma}_e^n \left[\frac{3}{2\tilde{q}} \left(\frac{\tilde{\sigma}_\theta - \tilde{\sigma}_r}{2} \right) + \frac{\mu}{2} \right] \tag{17}$$

$$\frac{1}{2}(\tilde{u}' + ns\tilde{v}) = \tilde{\sigma}_e^n \left[\frac{3}{2\tilde{q}} \tilde{\sigma}_{r\theta} \right] \tag{18}$$

Thus, the governing system consists of five equations (12), (13) and (16)–(18), with five unknown functions (three stress components and two displacements). The expressions for $\tilde{q}$ and $\tilde{\sigma}_e$ are given in (8) and (10) in algebraic form which, in fact, leaves us with a coupled system, of homogeneous ordinary differential equations, of the fourth order.

To complete the formulation we need four boundary conditions for the field variables. To this end we assume a symmetric pattern of indentation with equal friction along the walls $\theta = \pm(\pi - \alpha)$. The kinematic boundary condition

$$\tilde{v} = 0 \quad \text{at } \theta = \pm(\pi - \alpha) \tag{19}$$

is quite obvious, but it is less clear what friction condition should be imposed at the walls. One possibility is to take the Coulomb friction law (accounting for stresses sign convention and expecting $\tilde{\sigma}_\theta$ to be negative along the walls)

$$\tilde{\sigma}_{r\theta} = \pm f \tilde{\sigma}_\theta \quad \text{at } \theta = \pm(\pi - \alpha) \tag{20}$$

where f the Coulomb friction coefficient. However, in plastic forming processes (Durban, 1999) it is customary to model surface frictional contact with the Prandtl friction factor m which determines the relative contribution of surface shear stress to the effective Mises stress,

$$\tilde{\sigma}_{r\theta} = \pm m \tilde{q} \quad \text{at } \theta = \pm(\pi - \alpha) \tag{21}$$

Combining that condition with (8) we find that for a perfectly rough wall the friction factor m attains its highest possible value

$$m = m_{\max} = \left(\frac{1 - \mu^2/9}{3} \right)^{1/2} \tag{22}$$

In the same spirit we may consider the porosity friction factor ρ through the wall friction law

$$\tilde{\sigma}_{r\theta} = \pm\rho\tilde{\sigma}_{\mathrm{e}} \quad \text{at } \theta = \pm(\pi - \alpha) \tag{23}$$

with the effective stress given by (10). Thus, while the friction factor m reflects the influence of plasticity on wall friction, we may regard the porosity friction factor ρ as a measure of the coupling between pressure sensitivity, level of plastification and wall friction. Of course, for the Mises solid ($\mu = 0$) where $\tilde{\sigma}_{\mathrm{e}} = \tilde{q}$ we have $\rho \equiv m$.

Put differently, we have from (21) and (23) that along the walls of the indentor

$$m\tilde{q} = \rho\tilde{\sigma}_{\mathrm{e}} \tag{24}$$

Combining that relation with (9) and (10) gives the hydrostatic stress at the walls

$$\mu\tilde{\sigma}_{\mathrm{h}} = \left(\frac{m-\rho}{m}\right)\tilde{\sigma}_{\mathrm{e}} \tag{25}$$

implying a compressive hydrostatic environment when $\rho > m$.

It is instructive to examine the relations between the three measures of friction (f, m, ρ) as defined in (20), (21) and (23). To this end, we note from (8) and (21) that

$$\frac{\tilde{\sigma}_r - \tilde{\sigma}_\theta}{2} = (m_{\max}^2 - m^2)^{1/2}\tilde{q} \quad \text{at } \theta = \pm(\pi - \alpha) \tag{26}$$

where, in accordance with numerical observations and the physics of the problem, we have taken the positive root in (26). Eliminating now $\tilde{\sigma}_r$ between (10) and (26), and using (20) and (21) with (24), gives the following relation among the three measures of friction

$$\rho = \frac{mf}{[3m_{\max}^2 + \mu(m_{\max}^2 - m^2)^{1/2}]f - \mu m} \tag{27}$$

The friction factor m varies in the range $0 \leqslant m \leqslant m_{\max}$. For a smooth wall both f and ρ will vanish as well, while for a perfectly rough wall we find from (27)

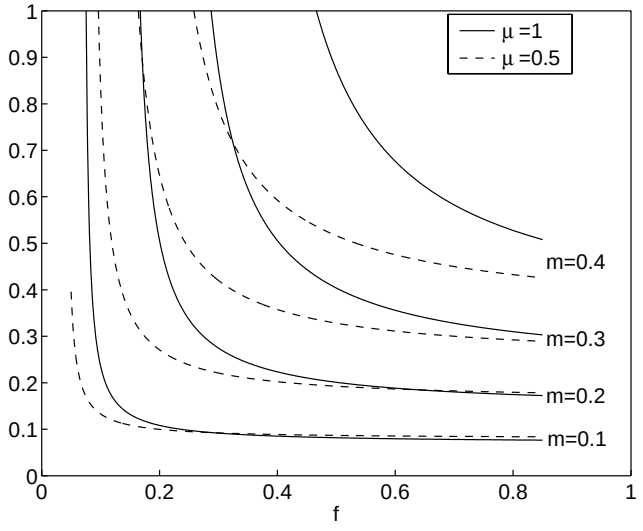

Fig. 2. Permissible pairs of Coulomb friction coefficient f and porosity friction ρ, at different levels of Prandtl friction factor m, for $\mu = 0.5$ and $\mu = 1$. A compressive hydrostatic environment exists for $\rho > m$.

$$\rho = \frac{f}{3m_{\max} f - \mu} \tag{28}$$

providing the lower bound $\mu/3m_{\max}$ on the Coulomb friction coefficient, and the lower bound $1/3m_{\max}$ on the porosity friction factor. Likewise, we have from (27) the two lower bounds

$$f > \frac{\mu m}{3m_{\max}^2 + \mu(m_{\max}^2 - m^2)^{1/2}} \quad \rho > \frac{m}{3m_{\max}^2 + \mu(m_{\max}^2 - m^2)^{1/2}} \tag{29}$$

for any permissible value of the friction factor m.

Fig. 2 displays typical curves for permissible pairs (f, ρ) at different levels of μ and m. The lower bounds (29) can be recognized as the asymptotes of the hyperbola (27) when either ρ or f become very large. Specific pairs (f, ρ) are determined by geometry (α), hardening (n), pressure sensitivity (μ), and friction factor (m).

3. Numerical results and discussion

The eigensystem (12), (13) and (16)–(18), along with the boundary conditions (19) and (21) has been solved numerically. A Galerkin type finite element scheme has been employed to trace the strongest permissible stress singularity $(-s)$ along with the associated profiles of the field variables. It is clear that Eqs. (12) and (13), together with the axis boundary conditions

$$\tilde{v} = 0 \quad \tilde{\sigma}_{r\theta} = 0 \quad \text{at } \theta = 0 \tag{30}$$

imply that the pattern of indentation must be symmetric. Thus the principal stresses $\tilde{\sigma}_r$ and $\tilde{\sigma}_\theta$ are even functions while the shear stress $\tilde{\sigma}_{r\theta}$ is an odd function. The domain of integration is from $\theta = 0$ (which in fact can be regarded as a smooth wall) to $\theta = \pi - \alpha$ where conditions (19) and (21) have to be satisfied. Boundedness of displacement components as $r \to 0$ and existence of stress singularities dictate the range

$$-\frac{1}{n} < s < 0 \tag{31}$$

for the eigenvalues. All field variables have been scaled by imposing wall reference pressure $\tilde{\sigma}_\theta(\pi - \alpha) = -1$. Numerical results have been checked against Mises solid $(\mu = 0)$ data detailed in Durban and Rand (1991).

Fig. 3 displays the variation of the stress singularity with the pressure sensitivity parameter μ for a wedge with semiangle $\alpha = 30°$ and smooth walls. It is clearly seen that the singularity level decreases with increasing hardening exponent n and shows little sensitivity to the plastic parameter μ. Also, as n increases, the singularity approaches the lower bound in (31).

The influence of friction factor m on the singularity level is illustrated in Fig. 4, again for a semiangle of $\alpha = 30°$, with two hardening exponents ($n = 1$, 3) and for a few values of μ. By comparison with Fig. 3 the influence of μ on s is more pronounced at higher values of wall friction. Recall that the friction factor m cannot exceed $m_{\max}$ of (22) which is $1/\sqrt{3} = 0.577$ for $\mu = 0$ and $2\sqrt{2}/3\sqrt{3} = 0.544$ for $\mu = 1$. The main observation from Fig. 4 is that wall friction reduces stress singularity, particularly at low values of the hardening exponent.

As expected, sharper wedges (smaller α) induce stronger singularities in the near tip plastic zone (Fig. 5). Furthermore, the curves in Fig. 5 suggest the existence of a critical wedge angle where the singularity vanishes altogether (this happens approximately for $\alpha \approx 60°$ with $m = 0.5$ and $\alpha \approx 90°$ with $m = 0$). At the other extreme, for very small wedge angles, the level of singularity in Fig. 5 is nearly independent of both m and μ.

A comparison between the three measures of surface friction is given in Fig. 6 which shows the variation of f and ρ with m for a "linear" solid, with $n = 1$, and wedge semiangle of $\alpha = 30°$. Both f and ρ increase with m but while f decreases with μ, the porosity friction factor ρ increases with μ. A similar observation

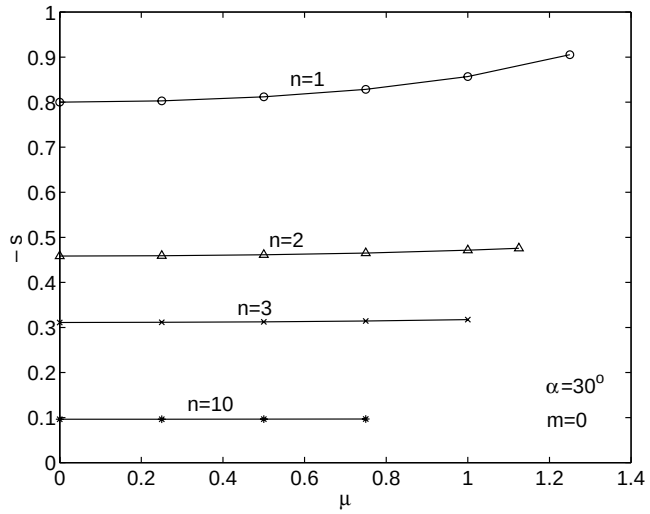

Fig. 3. Variation of stress singularity s with pressure sensitivity μ for $\alpha = 30°$ and $m = 0$.

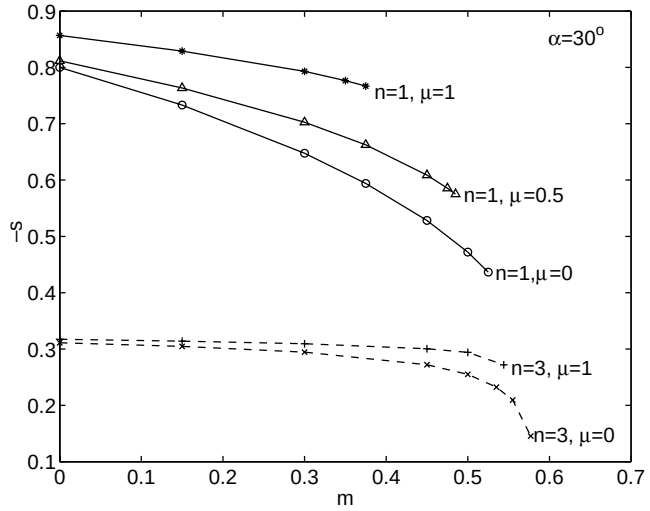

Fig. 4. Influence of friction factor m on singularity level s for a wedge with $\alpha = 30°$.

follows from Fig. 7 with $n = 3$. Both figures are compatible with the friction chart of Fig. 2, and in all cases $\rho > m$, ensuring by (25) a compressive hydrostatic environment. For $\mu = 0$ we have in Figs. 6 and 7 the straight lines $\rho = m$ of a Mises solid.

Illustrative examples of the stress profiles are shown in Fig. 8 for $n = 1$ and in Fig. 9 for a nearly perfectly plastic material with $n = 20$. Displacement and strain profiles, with the same parameters as in Fig. 8 are displayed in Figs. 10 and 11, respectively.

Contours of constant effective stress are displayed in Figs. 12 and 13 for a wedge with $\alpha = 30°$. Notice the decrease in size of the active plastic zone in Fig. 12 with increasing μ. In Fig. 13, with $n = 20$ the effective

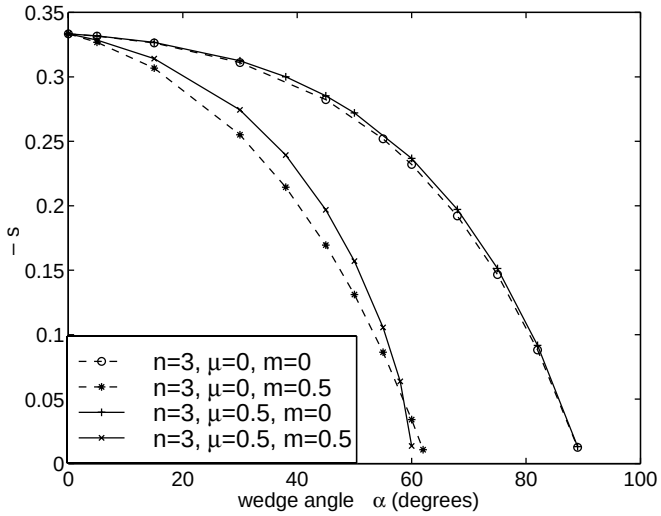

Fig. 5. Variation of stress singularity s with wedge angle α for $n = 3$. Singularity vanishes at critical wedge angles.

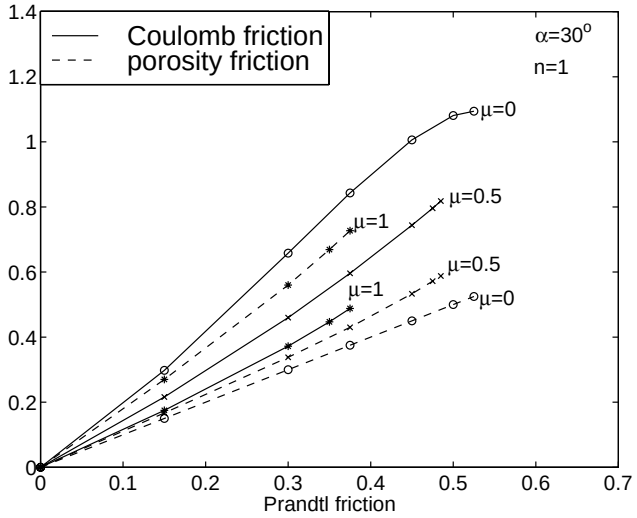

Fig. 6. Variation of Coulomb friction coefficient f and porosity friction factor ρ with Prandtl friction factor m, for $\alpha = 30°$ and $n = 1$.

stress contour approaches the slip lines orientations of perfect plasticity ($n \to \infty$). The decrease in size of the active plastic zone in Fig. 13 is pronounced with the scaling of the axes by 10^{-14}.

The influence of wall friction on boundary layer build up is clearly shown in Fig. 14, for the case of indentation by a rigid knife ($\alpha = 0$). A strong wall roughness either increases the shear stresses or an effective Mode I component of the stress intensification leading to a larger plastic zone. At high levels of the hardening exponent ($n = 20$) the slip line pattern is approached again with a friction boundary layer near rough walls (Fig. 15).

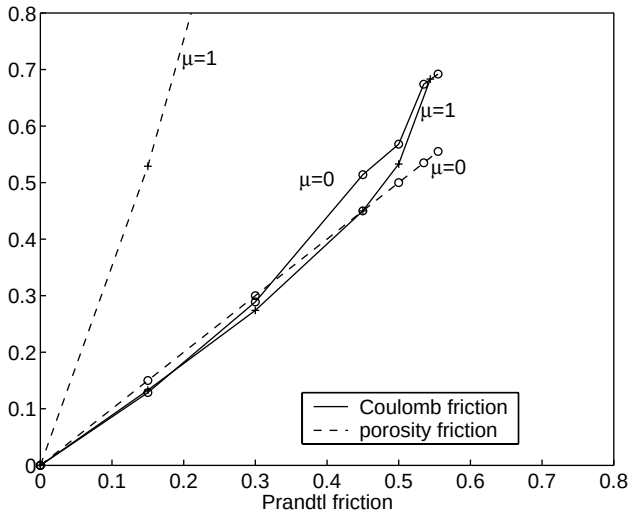

Fig. 7. Variation of Coulomb friction coefficient f and porosity friction factor ρ with Prandtl friction factor m, for $\alpha = 30°$ and $n = 3$.

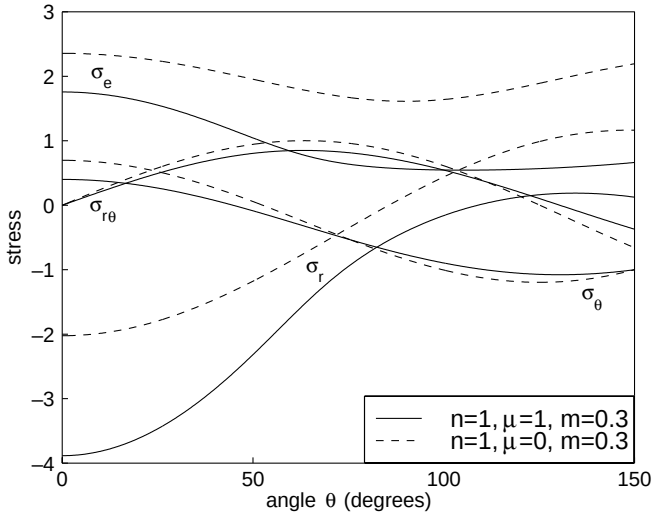

Fig. 8. Circumferential stress profiles for a "linear" solid with $n = 1$, $\alpha = 30°$.

4. Concluding comments

The near tip singular plastic field induced by indenting a wedge into a pressure sensitive solid exhibits considerable dependence on μ, particularly at higher levels of wall roughness. Stresses are more singular than for the Mises solid, though the difference is less pronounced at large values of the hardening index.Wall friction can be imposed by any of the three different measures, namely the Coulomb friction coefficient f, the Prandtl friction factor m or the porosity friction factor ρ. These three measures are

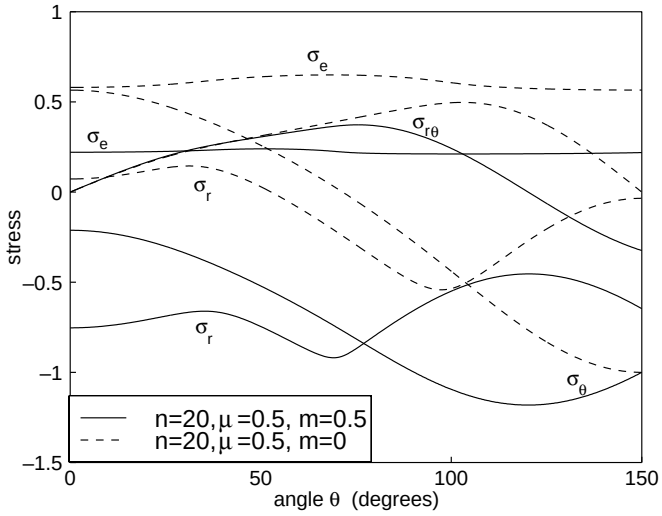

Fig. 9. Circumferential stress profiles for a nearly perfectly plastic solid with $n = 20$, $\alpha = 30°$.

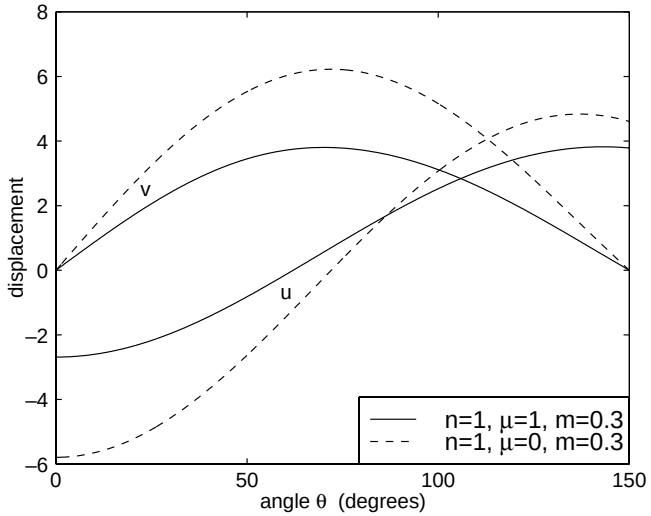

Fig. 10. Circumferential displacement profiles for $n = 1$, $\alpha = 30°$.

connected by relation (27) with the degenerate equality $\rho = m$ when $\mu = 0$. In this study we have chosen the Prandtl friction factor m as the prime parameter to describe surface friction. That measure has the advantage of being bounded by $0 \leqslant m \leqslant m_{\max}$, while both f and ρ can increase indefinitely. For given m, f appears to decrease with μ while ρ increases with μ.

For sufficiently low levels of friction, both f and ρ vary almost linearly with m and hydrostatic compression is ensured by $\rho > m$. However, ahead of the wedge along the penetration axis ($\theta = 0$) the circumferential strain ϵ_θ remains positive (Fig. 11).

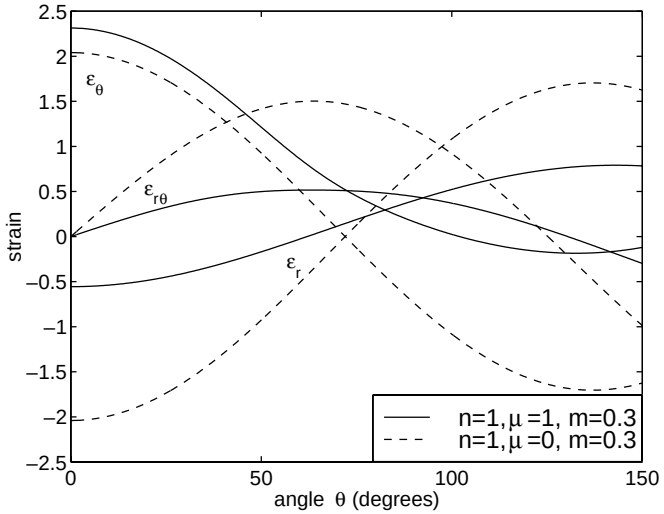

Fig. 11. Circumferential strain profiles for $n = 1$, $\alpha = 30°$.

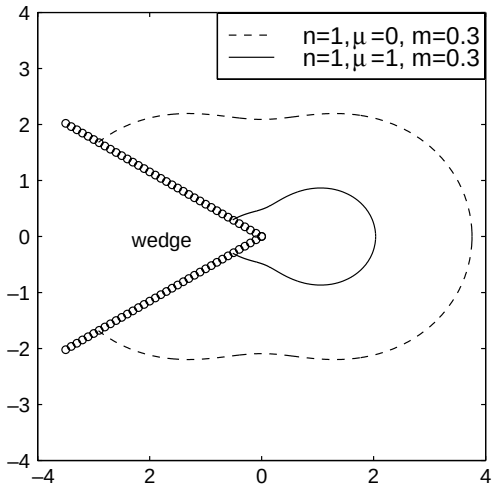

Fig. 12. Effective stress contours for $n = 1$, $\alpha = 30°$.

When the hardening exponent becomes very large, the contours of effective stress approach the shape of narrow concentrated zones in accordance with slip line theory for perfect plasticity. A boundary layer build up is observed near the walls when surface friction increases.

The near tip singular plastic field analysis can be applied to assess the average pressure required in wedge indentation. To this end we assume that at a distance $r = a$ along the walls the effective stress equals a nominal yield stress Y. Thus, from $(6)_3$

$$a^{s}\tilde{\sigma}_{e}(\pi - \alpha) = Y \tag{32}$$

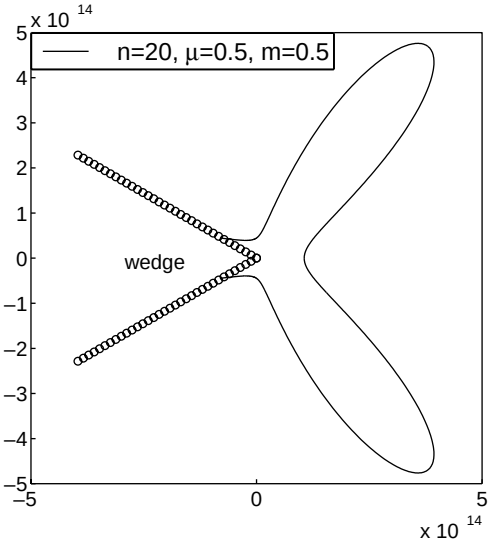

Fig. 13. Effective stress contours for $n = 20$, $\alpha = 30°$.

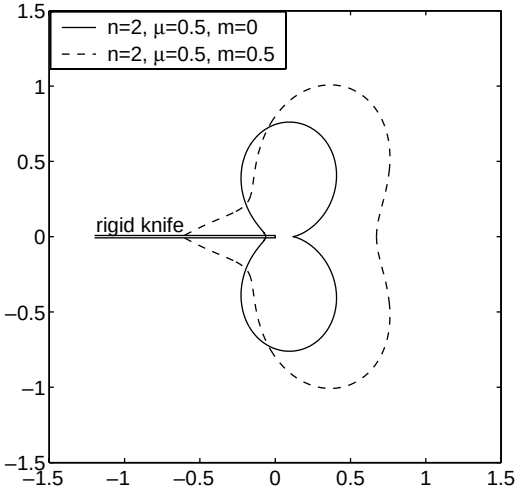

Fig. 14. Influence of wall friction on boundary layer build up for a rigid knife with $n = 2$.

The total resisting force F acting on the wedge tip from $r = 0$ to $r = a$ is given by

$$F = -2\int_0^a (\sigma_\theta \sin\alpha + \sigma_{r\theta}\cos\alpha)\,\mathrm{d}r = -\frac{2a^{s+1}}{1+s}(\tilde{\sigma}_\theta \sin\alpha + \tilde{\sigma}_{r\theta}\cos\alpha)_{\theta=\pi-\alpha} \tag{33}$$

in view of (5). Dividing F by the area projection $2a\sin\alpha$ and eliminating a^s through (32), gives the average penetrating pressure, over the singular plastic field,

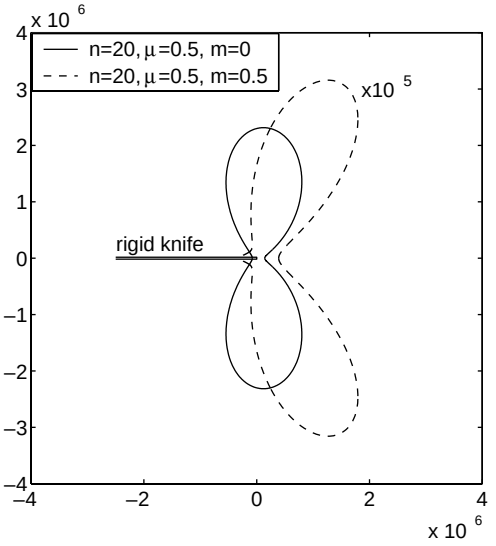

Fig. 15. Influence of wall friction on boundary layer build up for a rigid knife with $n = 20$. Note that for $m = 0.5$ the size of the contour was magnified by 10^5.

$$P = -\frac{Y}{1+s}\left(\frac{\tilde{\sigma}_\theta \sin\alpha + \tilde{\sigma}_{r\theta}\cos\alpha}{\tilde{\sigma}_e \sin\alpha}\right)_{\theta=\pi-\alpha} \tag{34}$$

This can be rewritten, with the aid of friction measures, as

$$P = C_D Y \tag{35}$$

where the indentation index C_D is defined by

$$C_D = \frac{\rho(1+f\cot\alpha)}{(1+s)f} \tag{36}$$

It may be argued, on intuitive ground, that (35) and (36) provide an upper bound on the actual value of the penetrating pressure since in our model elastic response is eliminated by the assumption of a rigid/plastic model. Just to give a few examples, for $\alpha = 30^\circ$ and $n = 3$, we have for the Mises solid ($\mu = 0$) the following representative values: $C_D(f = 0.1) = 1.93$, $C_D(0.2) = 2.07$ and $C_D(0.3) = 2.25$. These figures are comparable with available data from slip line theory (Grunsweig et al., 1954). While no attempt is made here to explore relation (36) any further, it is worth mentioning that with ρ given in (27) the indentation index C_D can be expressed in the form

$$C_D = \frac{m(1+f\cot\alpha)}{(1+s)[3m_{\max}^2 + \mu(m_{\max}^2 - m^2)^{1/2}]f - \mu m} \tag{37}$$

Now, for relatively large wedge angles and large n we have that $|s| \ll 1$. Adding the assumptions that $m^2 \ll m_{\max}^2$ and, within that range of parameters, $m \approx f$, we arrive at the useful approximation

$$C_D \approx \frac{1+f\cot\alpha}{3m_{\max}^2 + \mu m_{\max} - \mu} \quad n \gg 1 \quad m^2 \ll m_{\max}^2 \tag{38}$$

This relation can be further simplified for small values of μ, by (22), resulting in

$$C_D \approx \frac{1 + f\cot\alpha}{1 - (1 - 1/\sqrt{3})\mu} \quad \mu^2 \ll 9 \tag{39}$$

Indicating that indentation pressure increases with pressure sensitivity. Approximate formulae of this nature are helpful in estimating the required indentation pressure in plane strain conditions. This approximation is expected to be valid in the range of $n > 10$ and $m < 0.1$ along with $\mu < 1$.

Acknowledgements

The authors wish to thank Schlumberger Cambridge Research for supporting this research. Part of this study was supported by the fund for promotion of research at the Technion. D.D. wishes to acknowledge the support of the Sydney Goldstein Chair in Aeronautical Engineering.

References

De Boer, M.P., Gerberich, W.W., 1996. Microwedge indentation of the thin film fine line—I. Mechanics. Acta Mater. 44, 3169–3175.

Durban, D., 1999. Friction and singularities in steady penetration. In: Durban, D., Pearson, J.R.A. (Eds.), Non-linear Singularities in Deformation and Flow. Kluwer Academic Publishers, pp. 141–154.

Durban, D., Papanastasiou, P., 1997. Elastoplastic response of pressure sensitive solids. Int. J. Numer. Anal. Meth. Geomech. 21, 423–441.

Durban, D., Rand, O., 1991. Singular fields in plane-strain penetration. J. Appl. Mech. 58, 910–915.

Grunsweig, J., Longman, I.M., Petsch, N.J., 1954. Calculations and measurements of wedge indentation. J. Mech. Phys. Solids 2, 81.

Huang, H., Damjanac, B., Detournay, E., 1998. Normal wedge indentation in rocks with lateral confinement. Rock Mech. Rock Engng. 31, 81–94.

Papanastasiou, P., 1999. The effective fracture toughness in hydraulic fracturing. Int. J. Fract. 96, 127–147.

Tordesillas, A., Shi, J., 1998. Frictional indentation of dilatant granular materials. Proc. Roy. Soc. 455, 261–283.